Far-field outdoor experimental demonstration of down-looking synthetic aperture ladar

Guangyuan Li (李光远)[1,2], **Zhiyong Lu** (卢智勇)[1], **Yu Zhou** (周 煜)[1],
Jianfeng Sun (孙建锋)[1,*], **Qian Xu** (许 倩)[1], **Chenzhe Lao** (劳陈哲)[1,2],
Hongyu He (贺红雨)[1,2], **Guo Zhang** (张 国)[1,2], **and Liren Liu** (刘立人)[1]

[1]*Key Laboratory of Space Laser Communication and Detection Technology, Shanghai Institute of Optics and Fine Mechanics, Chinese Academy of Sciences, Shanghai 201800, China*
[2]*University of Chinese Academy of Sciences, Beijing 100049, China*
Corresponding author: sunjianfengs@163.com

A specific system structure of down-looking synthetic aperture imaging ladar (SAIL) is given, and a far-field experiment over 6 km of down-looking SAIL under this system design is carried out. The down-looking SAIL can overcome the influence of atmospheric turbulence to a great extent. By applying this system design, it also has advantages in self-compensating phase modulation. A fine image is obtained after aligning in the orthogonal direction and phase error compensation in the travel direction based on a dominant scatterer. The achieved imaging resolutions in the two dimensions are both better than 5 cm.

OCIS codes: 280.6730, 280.3640, 100.2000, 100.3010, 110.0110.
doi: 10.3788/COL201715.082801.

Synthetic aperture imaging ladar (SAIL) has the capability of getting high-resolution and two-dimensional (2D) active imaging at a large distance in the side-looking mode, which has become an interesting area of research. A number of laboratory experiments and flight demonstration of side-looking SAILs have been reported[1–7]. Additionally, due to the quite large effects of atmospheric turbulence and the mechanical dither of the platform on imaging, some compensation algorithms are used to obtain better imaging results[8,9].

Down-looking SAIL was reported[10] by the Shanghai Institute of Optics and Fine Mechanics, Chinese Academy of Sciences. In recent years, laboratory and outdoor experiments of down-looking SAIL have been performed by Luan *et al.*[11,12]. In 2016, an airborne experiment was done, and a fine image with high quality and a large field of view over 3 km was obtained[13]. Based on the principle of down-looking SAIL, Lu *et al.* proposed and verified a static-mode down-looking SAIL[14]. Zhang *et al.* proposed a spotlight-mode down-looking SAIL and demonstrated it in the laboratory[15]. Down-looking SAIL has advantages of a larger field of view and can overcome the influence of atmospheric turbulence to a great extent.

In the past, the farthest imaging distance of side-looking SAIL and down-looking SAIL was about 3 km, and the best resolution was 5 cm by the Institute of Electrics, Chinese Academy of Sciences. In a flight experiment by Lockheed Martin Coherent Technologies, the imaging distance was 1.6 km, and the resolutions were 2 cm × 3.3 cm[5]. As the imaging distance was far, the propagation time was relatively longer, the chirp signal of side-looking SAIL would change, and the echo phase was unstable due to the severe influence of atmospheric turbulence.

In this Letter, a far-field outdoor experiment, whose imaging distance was over 6 km, was done, and a fine resolution was obtained. The down-looking SAIL was mounted on a rotary table, and a synthetic aperture was implemented by the rotation of the rotary table. The system design of down-looking SAIL could obtain a very high phase modulation speed in the orthogonal direction, which is very important to high-speed imaging. At the same time, based on the rotation direction of the rotary table and galvanometer mirror, side-to-side vibrations of the galvanometer mirror would happen. The phase modulation module had a good self-compensating function and could eliminate the vibrational influence. Due to the self-heterodyne detection, the system effectively reduced the influence from atmospheric turbulence. However, it was difficult to guarantee the uniform velocity of the rotary table. This would lead to a lot of changes in the far field of the light spot and then affect the imaging quality. Therefore, it was necessary to compensate the signal based on a dominant scatterer.

A schematic of the down-looking SAIL system is shown in Fig. 1. The down-looking SAIL, which consists of a transmitter and a receiver, is mounted on the rotary table (R), as shown in Fig. 2. The transmitter is composed of a laser source, one half-wave plate (B1), one phase modulation module, one rotary table, and a main lens (M1). The phase modulation module is comprised of one half-wave plate (B2), four quarter-wave plates (H1, H2, H3, and H4), two cylinder lenses (L1 and L2), two polarization beam splitters (PBSs) acting as a splitter and a combiner, one mirror, and one galvanometer mirror. The *y*-direction cylinder lenses L1 and L2 are placed on the focal plane of the main lens and are used to generate spatial quadratic phase in the azimuthal direction.
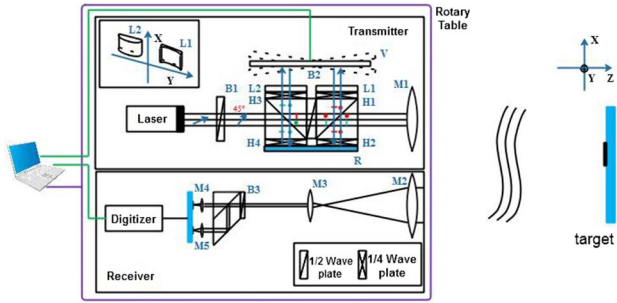
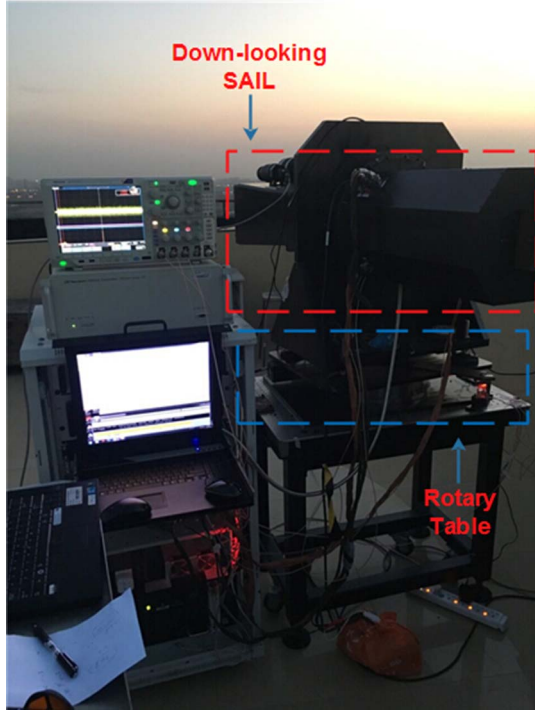Fig. 1. Experimental structure for down-looking SAIL.

Fig. 2. Outdoor experimental photo of down-looking SAIL.

The vibration of the galvanometer mirror is used to produce sinusoidal-phase modulation in the orthogonal direction. The receiver is composed of a receiving telescope (M2 and M3), a half-wave plate (B3), one PBS, two mini-lenses (M4 and M5), a balanced receiver, and a digitizer. The digitizer in the receiver is connected to and controlled correctly by the PC.

The galvanometer mirror, a part of the phase modulation module, is shown in Fig. 3. When the galvanometer mirror made a sinusoidal vibration, its maximum vibrational angle was A^{in}, and its frequency was f. The rotation direction (y-direction in Fig. 1) of the down-looking SAIL would generate a side-to-side vibration. The side-to-side vibrational angle was normally quite small, as shown in Fig. 3, and was named θ. L_v was the distance from the base of the galvanometer to the bottom of the optical spot.
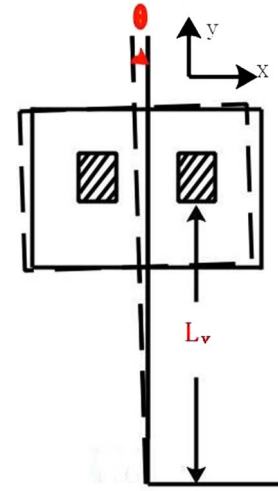

Fig. 3. Errors of the phase modulation module: side-to-side vibrant angle.

In this situation, the inner optical fields at the focal plane of the main lens could be expressed as follows:

$$e_H^{\mathrm{in}}(x,y) = C\mathrm{rect}\left\{\frac{[(x+x_l)-(L_v+y)\theta]\cos\theta}{L_x^{\mathrm{in}}}\right\}$$
$$\mathrm{rect}\left(\frac{y}{L_y^{\mathrm{in}}}\right)\mathrm{rect}\left(\frac{t_f}{T_f}\right)$$
$$\exp\left\{j\frac{2\pi}{\lambda}[(x+x_l)-(L_v+y)\theta]\cos\theta A^{\mathrm{in}}\sin(2\pi f t_f)\right\}$$
$$\exp\left(j\frac{\pi}{\lambda}\frac{y^2}{R_1^{\mathrm{in}}}\right), \tag{1}$$

$$e_V^{\mathrm{in}}(x,y) = C\mathrm{rect}\left\{\frac{[(x+x_l)+(L_v+y)\theta]\cos\theta}{L_x^{\mathrm{in}}}\right\}$$
$$\mathrm{rect}\left(\frac{y}{L_y^{\mathrm{in}}}\right)\mathrm{rect}\left(\frac{t_f}{T_f}\right)$$
$$\exp\left\{-j\frac{2\pi}{\lambda}[(x+x_l)+(L_v+y)\theta]\cos\theta A^{\mathrm{in}}\sin(2\pi f t_f)\right\}$$
$$\exp\left(j\frac{\pi}{\lambda}\frac{y^2}{R_1^{\mathrm{in}}}\right). \tag{2}$$

Here, $L_x^{\mathrm{in}} \times L_y^{\mathrm{in}}$ is the size of the inner beam, t_f is the fast scanning time, T_f is the width of the sampled time in the orthogonal direction, $(x+x_l)A^{\mathrm{in}}\sin(2\pi f t_f)$ is the phase in the x-direction relative to the x-position, x_l is the modulating position, with $x_l > L_x^{\mathrm{in}}/2$, and R_1^{in} is the equivalent quadratic radius of curvature.

Through the transmitting lens, the optical field on the target could be amplified with an amplification factor of $M = Z/F_M$, where F_M is the focal length of the main lens, and Z is the imaging distance. The reflected field from a target element at (x_p, y_p) was rotated 45° by the half-wave plate (B3) through the PBS, split into two channels by a

1×2 180° optical hybrid, and then injected into the balanced receiver.

The photocurrents resulting from the 1×2 180° optical hybrid could be expressed by a point-target radar equation, as follows (written in plural form):

$$
\begin{aligned}
&e(x_p, y_p; t_f, t_s) \\
&\approx C' \mathrm{rect}\left(\frac{x}{L_x}\right)\mathrm{rect}\left(\frac{y}{L_y}\right)\mathrm{rect}\left(\frac{t_f + t_r}{T_f}\right)\mathrm{rect}\left(\frac{t_s}{T_s}\right) \\
&\times \exp\left\{j\frac{\pi}{\lambda}\Big[4(x_p + M x_l)A\sin(2\pi f t_f)\Big]\right\} \\
&\times \exp\left\{j\frac{\pi}{\lambda}\left[\frac{(y_p - \beta t_s)^2}{R_1/2}\right]\right\}.
\end{aligned}
\tag{3}
$$

Here, c' includes all the factors of transmission, propagation, and optical-to-electrical conversion. $R_1 = M^2 R_1^{\mathrm{in}}$, $A = A^{\mathrm{in}}/M$, $L_x = M L_x^{\mathrm{in}}$, $L_y = M L_y^{\mathrm{in}}$, and t_s is the sampled time in the azimuthal direction from $-T_s/2$ to $T_s/2$, $t_\tau = 2Z/c$ is the time delay in the far field. When $t_r F_s < 1$, which means the discrete time number of the time delay is less than 1 point, the time delay can be neglected.

From Eq. (3), the vibration error was eliminated.

The image was focused by the Fourier transform in the orthogonal direction after linear processing and matched filtering in the azimuthal direction, as follows[16]:

$$
\begin{aligned}
&I(\xi, y) = \\
&C' F_{t_f \to \xi}\left\{\mathrm{rect}\left(\frac{t_f + t_\tau}{T_f}\right)\exp\left[\frac{j4\pi(x_p + M x_l)A(\alpha t_f + \phi)}{\lambda}\right]\right\} \\
&\times \mathrm{rect}\left(\frac{t_s}{T_s}\right)\exp\left[j\frac{\pi(y_p - \beta t_s)^2}{\lambda R_1/2}\right] \\
&\otimes \mathrm{rect}\left(\frac{t_s}{T_s}\right)\exp\left[-j\pi\frac{(\beta t_s)^2}{\lambda R_1/2}\right].
\end{aligned}
\tag{4}
$$

Here,

$$
\alpha = \left\{\sin\Big[\pi f(T_f/2 - t_\tau)\Big] + \sin\Big[\pi f(T_f/2 - t_\tau)\Big]\right\}/T_f
\tag{5}
$$

is the frequency linearity, and ϕ is a constant obtained through linear processing. $\otimes$ represents the convolution operation.

The simulation results are shown in Fig. 4. Four points were simulated, which were $(-100, 0)$, $(0, 0)$, $(50, 0)$, $(0, 100)$, and $(0, -50)$. The simulation parameters are same as those in the outdoor experiment and are presented in Table 1. As $t_\tau = 2ZF_s/c = 1417 \gg 1$, the time delay must be considered. Figure 4(a) is the compressed result in the orthogonal direction in consideration of the time delay, and Fig. 4(b) is the imaging result after two-dimensional compression.

In the outdoor experiment, as the forward and reverse data were both used when the galvanometer mirror vibrated, the sample frequency in the azimuthal direction
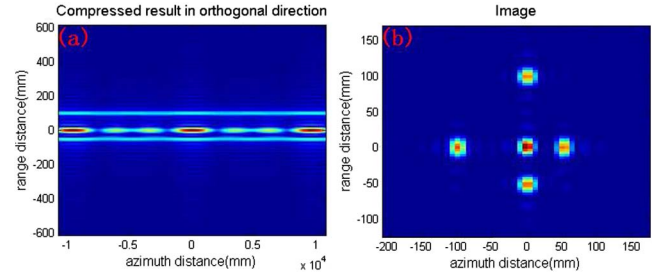

Fig. 4. Simulation results: (a) compressed image in the orthogonal direction and (b) the imaging result.

Table 1. System Parameters of Down-Looking SAIL

Parameters	Values
Wavelength λ	1030 nm
Vibrant angle	$\pm 7°$
Beam diameter	4 m × 4 m
Vibrant frequency	760 Hz
Focus length of launch/ receive lens	1.2 m
Imaging distance	6800 m
The rotation speed of the rotary table	0.1°/s
Modulation length	5 mm
Sampled frequency in orthogonal direction	31.25 MHz
Sampled frequency in azimuthal direction	1520 Hz
Cylindrical lens focal length	60 and −60 mm
Range × Azimuthal resolutions	28.8 mm × 21.9 mm
Laser power	30 W
Sampling duty cycle	58.91%

was double the vibrant frequency. The specific parameters are shown in Table 1.

As the distance between the mirror and the modulation module was very close, the beam passed through the cylindrical mirror two times; therefore, R_1^{in} was a quarter of the focal length.

According to the principle of down-looking SAIL, the far-field phase of the optical spot was the projection of the inner optical field with amplification factor M; therefore, the small jitter of the transmitting terminal and the small changing of the rotation velocity would cause a great change of the phase in the far field. At the same time, a longer distance needs more propagation time, during which the phase was more sensitive to the atmosphere. The processing procedure was as follow: (1) compressed in the orthogonal direction, (2) aligning in a line based

on a dominant scatterer, (3) calculating the phase errors function from the dominant scatterer, (4) making the phase errors compensate the original signal, and (5) compressed in the travel direction.

As Fig. 5(a) shows, four optical corner cubes are put in a cystosepiment as the target, which is placed on the building over 6 km. As previously mentioned, the time delay must be considered. The distances bet-ween the four optical corner cubes are also shown in Fig. 5(a). Figure 6 is the imaging result with compensation in the orthogonal direction. Obviously, Fig. 6(b) is aligning in a line. The imaging result after compensation based on a dominant scatterer is shown in Fig. 5(b), indicating that the resolutions for the two directions were both better than 5 cm.

In conclusion, the far-field (> 6 km) outdoor experiment of down-looking SAIL using the system design proposed in this Letter is demonstrated, and this design has a self-compensating phase modulation function, which eliminates the vibrational error of the galvanometer mirror. At the same time, it proves the advantage of down-looking SAIL in overcoming atmospheric turbulence. The resolutions in two dimensions are both better than 5 cm. Down-looking SAIL, which is a remote and high-resolution imaging tech-nique, has great application prospects.
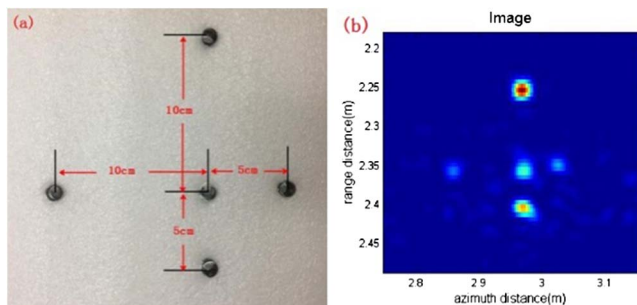
Fig. 5. Optical corner cube target and imaging result of down-looking SAIL over 6 km: (a) the optical corner cubes and (b) the imaging result.
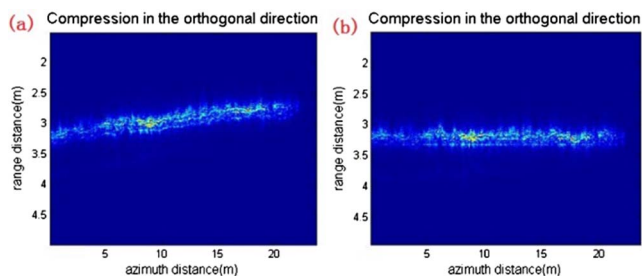

Fig. 6. Compressed image in the orthogonal direction over 6 km: (a) without alignment and (b) with alignment.

References

1. M. Bashkansky, R. L. Lucke, E. Funk, L. J. Rickard, and J. Reintjes, Opt. Lett. **27**, 1983 (2002).
2. S. M. Beck, J. R. Buck, W. F. Buell, R. P. Dickinson, D. A. Kozlowski, N. J. Marechal, and T. J. Wright, Appl. Opt. **44**, 7621 (2005).
3. Y. Zhou, N. Xu, Z. Luan, A Yan, L. Wang, J. Sun, and L. Liu, Acta Opt. Sin. **29**, 2030 (2009).
4. L. Liu, Y. Zhou, Y. Zhi, J. Sun, Y. Wu, Z. Luan, A. Yan, L. Wang, E. Dai, and W. Lu, Acta Opt. Sin. **37**, 09001121 (2011).
5. B. Krause, J. Buck, C. Ryan, D. Hwang, P. Kondratko, A. Malm, A. Gleason, and S. Ashby, in *Proceedings of OSA/CLEO/QELS* (2011), paper PDPB7.
6. J Wu, Z. Yang, Z. Zhao, F. Li, D. Wang, Y. Tang, Y. Su, and N. Liang, J. Infrared Millim. Waves. **32**, 00514 (2013).
7. Z. Zhao, J. Wu, Y. Su, N. Liang, and H. Duan, Chin. Opt. Lett. **12**, 091101 (2014).
8. D. E. Wahl, P. H. Eichel, D. C. Ghiglia, and C. V. Jakowatz, Jr., IEEE Trans. Aerosp. Electron. Syst. **30**, 827 (1994).
9. J. R. Fienup, Opt. Lett. **25**, 221 (2000).
10. L. Liu, Acta Opt. Sin. **32**, 0920002 (2012).
11. Z. Luan, J. Sun, Y. Zhi, Y. Zhou, L. Wang, and L. Liu, Acta. Opt. Sin. **34**, 0710003 (2014).
12. Z. Luan, J. Sun, Y. Zhou, L. Wang, M. Yang, and L. Liu, Chin. Opt. Lett. **12**, 111101 (2014).
13. Z. Lu, Y. Zhou, J. Sun, L. Luan, L. Wang, Q. Xu, G. Li, G. Zhang, and L. Liu, Chin. J. Laser **44**, 0110001 (2017).
14. Z. Lu, N. Zhang, J. Sun, Y. Zhou, Z. Luan, G. Cai, and L. Liu, Chin. Opt. Lett. **13**, 042801 (2015).
15. N. Zhang, Z. Lu, J. Sun, Z. Yu, Z. Luan, Z. Sun, G. Li, and L. Liu, Chin. Opt. Lett. **13**, 091001 (2015).
16. G. Li, J. Sun, Z. Lu, N. Zhang, G. Cai, Z. Sun, and L. Liu, Proc. SPIE **9617**, 96170N (2015).